The Global Atmosphere and Ocean System,
Vol. 9, No. 3, September 2003, pp. 97–120

Taylor & Francis
Taylor & Francis Group

IMPACT OF WAVES ON THE SEA DRAG: MEASUREMENTS IN THE BALTIC SEA AND A MODEL INTERPRETATION

XIAOLI GUO LARSÉN[a,*], VLADIMIR K. MAKIN[b]
and ANN-SOFI SMEDMAN[a]

[a]*Department of Earth Sciences, Uppsala University, Meteorology, Villavägen 16, S-75273, Uppsala, Sweden;* [b]*Royal Netherlands Meteorological Institute (KNMI), De Bilt, The Netherlands*

(Received 13 January 2003; Revised 28 April 2003; In final form 10 July 2003)

Measurements from the Baltic Sea and a wind-over-wave coupled model are used to study the wave impact on the sea drag. The study has been carried out for different wave conditions, namely a pure wind-sea, following-swell/ mixed sea and cross-swell/ mixed sea. Measurements reveal the fact that the sea drag is dependent on the sea-state. In stationary conditions and in the absence of severe cross-swell, swell reduces drag compared to wind-sea at the same wind speed. The cross-swell enhances the drag as compared to the following-swell case and the magnitude of the drag coefficient is increased with increasing the angle of swell propagation to the wind. It is shown that the agreement between the model results and measurements is good for pure wind-sea and stationary mixed-sea cases. Discrepancies occur at light winds, where most of the data represent pure swell conditions. During these pure swell conditions the data are characterized by a large variation of the drag coefficient. The variation is caused by mesoscale variability in the stress co-spectra, wind-cross-swell effects and nonstationarity in the wave and wind fields not represented in the model.

Keywords: Wind-sea; Baltic Sea; Wind-over-wave coupled model

1 INTRODUCTION

When wind blows over still water, waves will be generated and develop into a pure wind-sea. During this process, momentum is transferred from atmosphere to water. When the wind slows down and becomes slower than the wave propagation, it can no longer feed energy and momentum to the waves. Swell – waves traveling faster than the wind – originate. One might expect momentum to be transferred in an opposite direction, from swell to the wind. Correct estimation of the momentum flux is important not only for modeling the wave growth, but also it is a key issue in the study of the coupled atmosphere–ocean system.

Mixed wind-sea/swell or pure swell conditions are typical for the open ocean. Though it is believed that swell interacts weakly with the atmosphere – otherwise it will not have a chance to cross the oceans (e.g., Snodgrass *et al.*, 1966) – its overall impact

*Corresponding author. Tel.: +46-18-4717188. Fax: +46-18-551124. E-mail: xiaoli.guo@met.uu.se

ISSN 1023-6732 print: ISSN 1477-2779 online
DOI: 10.1080/10236730310001606308

could be significant especially in the tropics, where the atmosphere slowly accumulates momentum, heat and moisture and then releases it in other regions of the ocean.

Experimental and theoretical study of how the atmosphere and the ocean exchange momentum has a long history (e.g., reviews by Donelan, 1990; Geernaert, 1990; Smith *et al*., 1996). At present the exchange of momentum is quite well understood but only in the case of a pure wind-sea. A wind-over-waves coupling (WOWC) theory relates the surface stress (sea drag) directly to the properties of wind waves and peculiarities of their interaction with the wind. It explains the formation of the sea drag by the viscous friction mechanism, by the form drag due to the nonseparated sheltering mechanism and due to the airflow separation from equilibrium short gravity waves and from dominant waves at the spectral peak of the wave spectrum.

The exchange processes in the presence of swell are less understood. Only a few data sets of the stress directly measured under swell conditions exist (Donelan *et al*., 1997; Drennan *et al*., 1999a,b; Smedman *et al*., 1999, 2003), and a theory of the drag formation is lacking.

Field measurements have reported a very complicated variation of stress during pure swell conditions. Some studies, e.g. Dobson *et al*. (1994), failed to find any influence of swell. This is probably because their inertial dissipation method had presumed no swell influence. The transport terms in the turbulent kinetic budget, which were assumed to be negligible by the inertial dissipation method, have been found to be significant during swell conditions (e.g. Sjöblom and Smedman, 2002). Others, e.g. Smedman *et al*. (1999), Drennan *et al*. (1999b) and Grachev and Fairall (2001) have observed negative stress during strong following swell conditions. Donelan *et al*. (1997) and Drennan *et al*. (1999b) have reported significantly enhanced drag coefficients during cross-wind swell conditions, and even more at opposite-wind swells. The nonstationarity of the wind and wave field has also been found to be a possible factor to the variation of the drag coefficient (Rieder, 1997; Drennan *et al*., 1999b; Smedman *et al*., 2003).

In the present study, the measurements from an airsea interaction Östergarnsholm station and a wave rider buoy in the Baltic Sea are used to further explore the impact of waves on the sea drag with special attention to swell cases. Consecutive data sets from all seasons are selected. They provide wave conditions of a pure wind-sea, following-mixed sea/swell, and cross-mixed sea/swell. In total 16 separate runs were used providing a total of 345 sets of one-hourly values.

At the same time a wind-over-waves coupled model by Kudryavtsev and Makin (2001) (hereinafter KM2001) and Makin and Kudryavtsev (2002) (hereinafter MK2002) is used for data interpretation. Since the model assumes no swell impact on the sea drag for swell cases the discrepancies between the model and measurements will clearly reflect the difference in the impact given by a pure wind-sea and by swell on the stress.

The measuring site and the measurements are introduced in Section 2. The WOWC model will be briefly presented in Section 3. Results of comparison are given in Section 4. Conclusions are given in Section 5.

2 MEASUREMENTS

2.1 Measuring Site and Data

The atmospheric data used in this study are sampled at the site Östergarnsholm, which is shown in Fig. 1. This is a low flat island outside of the bigger island of

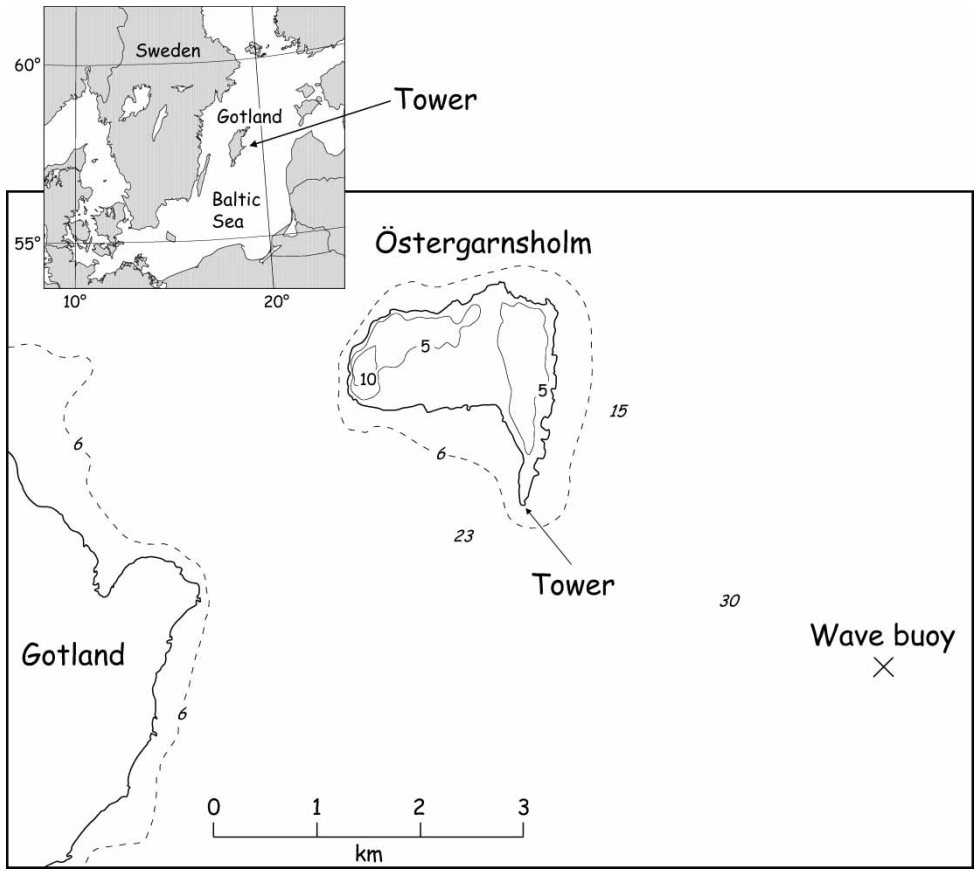

FIGURE 1 Map of the Baltic Sea (upper left), with a close-up of the site Östergarnsholm. Dashed lines are the contours of water depth, and solid lines on Östergarnsholm are the contours of height. The wave rider buoy is moored at 36 m, about 4 km southeast of the island.

Gotland in the Baltic Sea. At the southernmost tip of the island a 30 m high instrumented tower has been erected. The instruments for eddy-correlation measurements are Solent 1012R2 sonic anemometers (Gill Instruments, Lymington, United Kingdom), and the instruments for measuring the wind speed and the wind direction are light-weight cup anemometers and Styrofoam wind vanes. The sonic anemometers are placed at 9, 17 and 25 m above the tower base, and the 'profile' sensors at 5 levels at the heights of 6.9, 11.9, 14.3, 20.2 and 28.8 m. The distance between the tower base and the water level changes with synoptic conditions over the Baltic Sea and part of the North Sea areas. The actual measuring heights are calculated from the water level measurement at Visby harbor, which is located on the western coast of Gotland.

The sonic anemometers and the cup anemometers have been calibrated in a large wind tunnel and flow distortion correction matrices have been estimated for the sonic anemometers before they were installed on the tower (cf. Grelle and Lindroth, 1994). The turbulent data at Östergarnsholm is recorded at a frequency of 20 Hz. Virtual temperature and three orthogonal components of the wind are

obtained from the sonic signals. The 'profile' data are recorded at a frequency of 1 Hz. One hour averages of turbulent and 'profile' data are used in this study. Before calculating the variance and covariance, a 10 min running average was applied to the 20 Hz data to remove possible trends from the time series. This is the same as applying a high-pass filter with a cutoff frequency at about 10^{-3} Hz. One way to check if the 10 min running mean (or the cutoff frequency around 10^{-3} Hz) represents the total variance is to study the corresponding Ogive-curve. The Ogive-curve is the integrated co-spectrum $C_{\mathrm{Ogive}}(n) = \int_{n_h}^{n} nC_{uw}(n)d\ln n$, where n is the frequency, n_h is the high frequency limit, ~ 10 Hz and $n < n_h$. $C_{uw}(n)$ is the co-spectrum of the horizontal- and vertical wind components u and w, as a function of n. If the value of C_{Ogive} levels off for $n < 10^{-3}$ Hz then 10^{-3} Hz could be considered as a reasonable cutoff frequency. When using this criterion to the data set selected, it was found that for most data, the Ogive-curves do level off at the cutoff frequency $\sim 10^{-3}$ Hz. However, there are periods when this condition is not fulfilled, and this will be discussed in Section 4.

At normal sea level, the distance from the tower to the shoreline is about 5–20 m in the sector from northeast to southwest. The seafloor has an approximate slope of 1 : 30, though slightly different in different directions. The water depth is 50 m about 10 km away from the peninsula, reaching 100 m farther out. There is an undisturbed over-water fetch of more than 150 km in the wind direction sector about 80–220°. In this study we only use data with wind from this sector.

The measured turbulent fluxes originate from an upwind area. Smedman *et al* (1999) calculated the 'footprint' area (see details in the original paper) and found that for neutral conditions, at a height of 10 m, 90% of the measured flux originates from areas beyond 250 m, 50% from beyond 670 m, and 70% from areas between 250 and 1700 m. At a height of 18 m, the corresponding figures are 450 m, 1250 m, and 450–3200 m respectively. At a height of 26 m, the corresponding figures are 770 m, 1980 m and 770–5300 m.

The wave data used are obtained from a wave buoy moored about 4 km away from the tower in the direction of 115° where the water depth is about 40 m. The wave data are thus representative of wave condition in the upwind fetch. The wave buoy is owned and run by the Finnish Institute of Marine Research. The wave measurements have been taken semi-continuously. Wave data are recorded once an hour as a time series of 1600 s. A unidirectional spectrum is calculated from the time series, containing 64 frequency bands in the range of 0.025–0.58 Hz, with the peak frequency determined by a parabolic fit. The dominant direction in each frequency bin is also extracted (e.g. Figure 2a). The significant wave height H_s is calculated as 4 times the root mean square of the integrated wave spectrum over 0.050–0.58 Hz.

Figure 2 gives an example of the wave spectrum (1995-09-19). Figure 2(a) shows the wave direction during 1 h as a function of frequency n, together with the average wind direction. Figure 2(b) shows the energy density $S(n)$ as a function of frequency n and in Fig. 2(c), $\ln(n^4 S(n))$ is plotted against n. In Fig. 2(d), the plotted variables are: hourly average of the wind speed at 10 m U_{10}, the wind speed in the wave propagating direction U_c and the wave phase velocity for deep water c. All are plotted as a function of n, and c is calculated from the dispersion relation $c = g/(2\pi n)$.

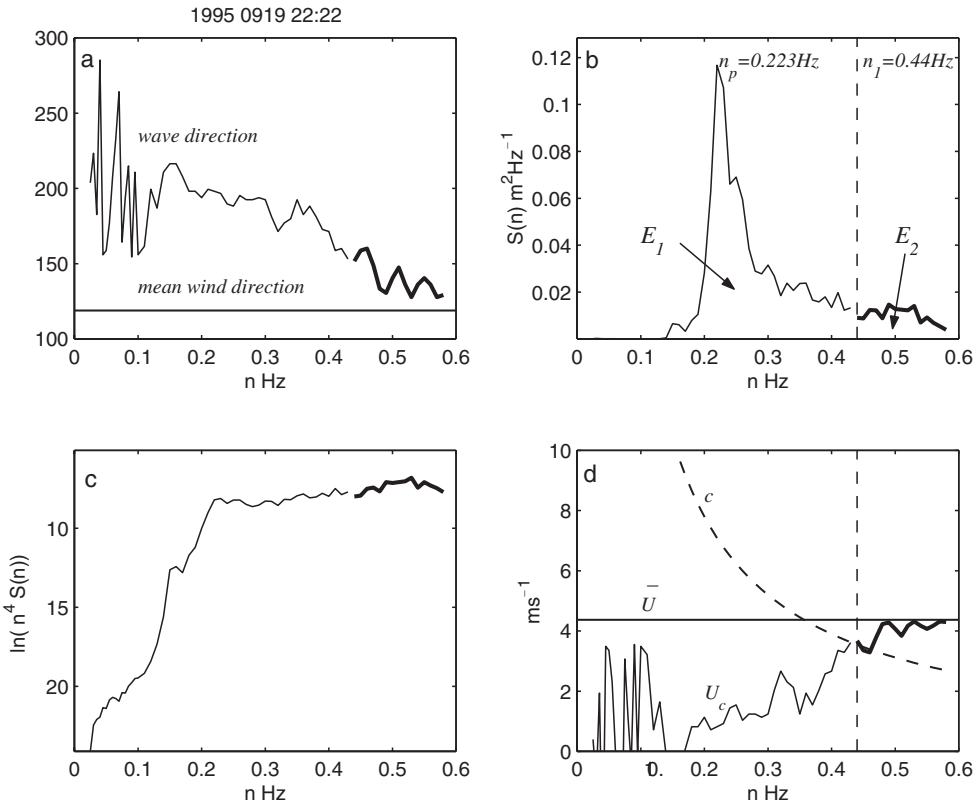

FIGURE 2 An example of a wave spectrum. (a) Mean wind direction during 1 h (straight solid line) and wave direction as a function of frequency n. (b) Energy density as a function of n. (c) $\ln(n^4 S(n))$ as a function of n. (d) Mean wind speed at 10 m (straight solid line), wind speed in the wave propagating direction $U_c = U\cos\alpha$, and wave phase velocity for deep water $c = g/(2\pi n)$, all plotted as functions of n. The vertical thin dashed line shows the frequency n_1 where $U_c = c$, and it divides the spectrum (b) into two parts. E_1 and E_2 are the integrated wave energy densities for longer wave regime (thin curve) and shorter wave regime (thick curves).

2.2 Data Grouping

There are two groups of data selected, one for a pure wind-sea (Group-1), and the other for a swell-dominant case (Group-2). Both groups contain long periods of data continuous in time, and they satisfy the following conditions:

1. There are complete meteorological and wave measurements,
2. Wind is from 80 to 220°,
3. Wind speeds at all levels are larger than 2 ms^{-1},
4. There is only one dominant peak in the wave spectrum,
5. Wave direction is about 80–220°.

Those long periods in the two groups are listed in Table I. When grouping data at different wave conditions in two groups, the parameter E_1/E_2 from Smedman *et al.* (2003) is used (see details in Table II). E_1 and E_2 are the integrated wave energy density

TABLE I List of the periods selected

Group	*Run*	*Periods*	*Length of the data* (h)
Group 1	1	9509 14–15 (14th to 15th, sep. 1995)	29
	2	9801 02	20
	3	9803 26–27	31
	4	9810 25–27	59
	5	9901 02–04	50
	6	9906 29–30	30
	7	9909 25–27	87
	8	9910 02	17
Group 2	9	9509 18–20	49
	10	9609 23	12
	11–13	9711 06, 08, 10–11	86
	14–15	9801 02–03, 19	28
	16	9811 10–12	50

TABLE II Classification of wave data according to E_1/E_2

Pure wind-sea (from Group-1)		$E_1/E_2 < 0.2$	
Swell-dominant (from Group-2)	Mixed sea	$0.2 \le E_1/E_2 < 4$	$n_p < n_1$
	Pure swell	$E_1/E_2 \ge 4$	

for the waves traveling faster than the wind (swell) and short slow moving waves actively interacting with the wind:

$$E_1 = \int_0^{n_1} S(n)\,dn \qquad E_2 = \int_{n_1}^{0.58} S(n)\,dn \quad n_1 = \frac{g}{2\pi U_{10}\cos\alpha}, \tag{1}$$

where α is the difference in the direction between the wind and the dominant waves (waves at the spectral peak of the wave spectrum), and n_1 is the frequency at which the wave phase velocity c derived for a deep water condition matches the wind speed at 10 m in the wave propagating direction (U_c); see the example given in Fig. 2(d). The vertical lines in Fig. 2(b) and (d) mark the frequency n_1 ($=0.44$ Hz during this hour). It divides the wave spectrum into two parts, marked with a thin solid curve and a thick solid curve, respectively.

The integrated energy densities for the two parts are E_1 and E_2 respectively. As can be seen the direction of the short waves is close to the mean wind direction. As shown by Smedman *et al.* (2003), there is a strong relationship between E_2 and U_{10}^2, but not between E_1 and U_{10}^2, demonstrating that the short waves are closely related to the local wind generation.

Data in Group-2 are classified further according to the difference in the direction between wind and the dominant waves, α. The details are listed in Table III.

Figure 2 represents a typical cross-swell case, with $E_1/E_2 = 6.93$, n_p (0.223 Hz) $< n_1$ (0.44 Hz), $c_p/U_c = 7.89$; wind direction 118.9°, average direction of the dominant wave 198°, and the direction difference 79.1°. c_p is the phase velocity at the spectral

TABLE III Classification swell/mixed sea data according to the direction difference between wind and dominant waves α

Following-swell/mixed sea (for simplicity called following-swell)	*Cross-swell/mixed sea (for simplicity called cross-swell)*	
$\alpha < 30^\circ$	$\alpha \geq 30^\circ$	$30 \leq \alpha < 40^\circ$
		$40 \leq \alpha < 60^\circ$
		$60 \leq \alpha < 82^\circ$

peak and it is calculated with consideration of the water depth h and the 'footprint weighting function' $F(x, z)$, see Smedman *et al*. (2003) for the details:

$$c_p = \int_0^\infty F(x, z) \cdot c_{p,1}(x) \cdot dx$$

Here $c_{p,1}$ is iterated from the dispersion relation

$$c_{p,1} = \frac{g}{\omega_p} \cdot \tanh\left(\frac{\omega_p h}{c_{p,1}}\right)$$

where ω_p is the radian peak wave frequency.

3 THE WIND OVER WAVE COUPLED MODEL

3.1 The Model Framework

In this section, the WOWC model of KM2001 and MK2002 is briefly described (for details the reader is addressed to the original papers). The model is based on the conservation equation for the stress τ in the marine atmospheric surface boundary layer:

$$\partial\tau/\partial z = 0, \tag{2}$$

which implies that the stress is constant over height. It is assumed that the wind is stationary, spatially homogeneous, its direction coincides with the mean direction of wave propagation, and the wave field (wave spectrum) is symmetrical relative to that direction. Under these conditions only one component of the stress is present, i.e. the downwind component.

At the surface τ contains three parts, namely τ^ν – the viscous stress, τ^w – the wave-induced stress supported by the nonseparated airflow (corresponding to nonbreaking waves) and τ^s – the stress supported by the airflow separation (corresponding to breaking waves). Far above the waves outside the wave boundary layer, i.e., at height where the impact of waves on the stress vanishes the stress is supported only by the turbulent stress $\tau^t = -\overline{u'w'}$, which is equal to the square of the friction velocity u_* so that $\tau \equiv \tau^t = -\overline{u'w'} = u_*^2$. The height of 10 m is assumed sufficient to neglect the stress supported by waves.

Integrating over the height the conservation equation for integral momentum is obtained

$$u_*^2 = \tau^\nu + \tau^w + \tau^s. \tag{3}$$

Equation (3) requires no details of the vertical variation of stresses. The model is based on Eq. (3).

τ^{ν} is obtained by requiring the smooth transition of the linear wind profile in the viscous layer (which is a few millimeters deep) and the assumed logarithmic wind profile above it:

$$U(z) = \frac{u_*}{\kappa} \ln \frac{z}{z_0}, \tag{4}$$

where $U(z)$ is the wind speed at height z, κ is the von-Karman constant, and z_0 is the roughness length for momentum.

τ^{w} is formed by the nonseparated airflow over a regular, nonbreaking wave. It is described traditionally by the wave-growth parameter (e.g. Plant, 1982), which depends on the roughness parameter and the friction velocity, and the wave energy spectrum.

τ^{s} is associated with the airflow separation from breaking waves when the sea surface is disrupted. It is parameterized in proportion to the pressure drop Δp on both sides of the crests of the breaking wave front. τ^{s} is supported by breaking waves from the *equilibrium range* (τ^{s}_{eq}) of the wave spectrum (KM2001) and by the dominant waves of the *spectral peak range* (τ^{s}_{d}) (MK2002). The separation stress can be also expressed in terms of the wave spectrum; the friction velocity and the roughness parameter (see KM2001, MK2002). KM2001 show that for a fully developed sea, τ^{s}_{eq} contributes significantly to the total stress, up to 50% at high wind speeds. MK2002 show that τ^{s}_{d} is negligible for a fully developed sea but significant for younger seas.

For a given wind speed U_{10} and the wave spectrum $B(k, \theta)$ (k is the wave number, and θ is the angle between wind and waves), the model provides the surface stress, which can be expressed in terms of the friction velocity ($\tau = u_*^2$) or the roughness parameter according to (4). The stress (friction velocity, roughness parameter) is defined by the wave spectrum $B(k, \theta)$. The wave spectrum in turn depends on u_*. Thus the wind waves and the atmospheric boundary layer are coupled in a self-consistent dynamical system, as shown in Fig. 3.

For young waves ($0.04 < c_p/U_c < 1.2$) to fully developed waves ($c_p/U_c \sim 1.2$) the model results have been shown (MK2002) to be in reasonable agreement with several field and laboratory measurements of the stress.

3.2 Description of Wave Spectrum

To obtain the stress the wave spectrum should be known. It can be described by an empirical model, by a physical model based on the energy balance equation, or just taken from observations. Here a composite model of the wave spectrum

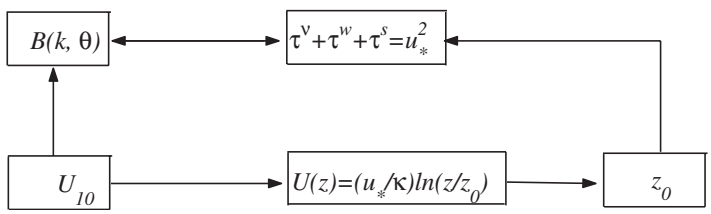

FIGURE 3 The self-consistent system of the model, with input of wind speed U_{10}.

(Kudryavtsev *et al*., 1999) which describes the energy density spectrum $B(k,\theta)$, in the full wave number range from a few millimeters up to the spectral peak, is used. It consists of two parts: the low wave number spectrum B_l ($0.1\,k_p < k < \sim 10\,k_p$), and the high wave number spectrum B_h ($k \gg k_p$)

$$B(k,\theta) = B_l(k,\theta) + B_h(k,\theta). \tag{5}$$

The shape of the high wavenumber spectrum B_h results from the physical model developed by Kudryavtsev *et al*. (1999). The model is based on the energy balance equation and accounts for wind input, viscous dissipation, dissipation due to wave breaking, and nonlinear three-wave interaction. The short waves support most of the sea drag (KM2001), which is why their description through a balance of physical mechanisms is crucial. The shape of the low wavenumber (at the spectral peak) B_l spectrum defined by the inverse wave age parameter U_{10}/c_p is given by the empirical model by Donelan *et al*. (1985).

Description of B_l through the empirical model of Donelan *et al*. (1985) is inappropriate for a swell case. That is why the measurements of the wave spectra are used directly as input to the model for swell cases. The wave spectra cover the frequency range 0.025–0.58 Hz, with the limit for the smallest wavelength of ~ 4.6 m. Thus the measured wave spectra are used for the low wave number regime B_l in (5), while the high wave number regime B_h remains the same as proposed in Kudryavtsev *et al*. (1999). Here it should be noted explicitly that the WOWC model used in the present study does not include any mechanism of swell interaction with the wind. Separation from dominant waves cannot occur from waves propagating faster than the wind, as explained in MK2002, while the growth rate parameter is set to zero. So, the model only deals with the wind-sea part of the swell-dominated cases $S(n > n_1)$ and assumes no influence from the *pure swell* part. The discrepancy between model and measurements in this case will clearly reflect the difference in the impact given by a pure wind-sea and by swell on the stress.

3.3 Model Input

The model was provided with the measured wind speed at 10 m height. In the case of a pure wind sea the model was provided with the peak frequency for the estimation of the inverse wave age parameter and the reconstruction of the spectral shape for B_l. The correspondence of the modeled and observed wave spectra was checked by comparing the modeled and observed significant wave heights. A good comparison was found. In swell cases the measured spectral shape for B_l is used. The model values of stress are then compared with stress measurements.

4 COMPARISON OF MEASURED AND CALCULATED STRESS

4.1 Statistical Parameters

The following statistical parameters are used when comparing the calculated and observed stress: correlation coefficient (r), root mean square error (rms error), and index of agreement (IOA) specified in the Appendix. Outliers are not included in the

statistics. Outliers are identified according to $|X_i - \overline{X}| > 3\sigma_X$, where X_i is the ith element of the array X, $\overline{X}$ is the mean value of X, and σ_X is the standard deviation of X.

The observed stress τ_{obs} is calculated from:

$$\tau_{\text{obs}} = \left[(-\overline{u'w'})^2 + (-\overline{v'w'})^2\right]^{1/2} \tag{6}$$

where $-\overline{u'w'}$ is the downstream stress and $-\overline{v'w'}$ is the crosswind stress. The modeled and observed drag coefficient C_D is

$$C_D = \tau_i / U_{10}^2 \tag{7}$$

where $i = [\text{obs, mod}]$.

The first order regression line and the standard deviation are shown in figures, where τ_{mod} is plotted against τ_{obs}. Ratio of the calculated and observed stress ($\tau_{\text{mod}}/\tau_{\text{obs}}$) and the standard deviation of the ratio are used in order to highlight small stress values, which are often overwhelmed by large stress values when standard statistical parameters are applied.

The results of the comparisons are listed in Table IV for a pure wind-sea, cross-swell and following-swell cases. Ranges of the wind speed and the wave age parameter c_p/U_c are also given. For all cases the stability of the atmosphere was close to neutral so that no stability correction was applied to the data.

4.2 Pure Wind-sea

For the pure wind-sea case, the wind speed U_{10} varies between ~ 6 and $\sim 17\,\text{ms}^{-1}$. The regime is characterized by the wave age parameter $c_p/U_{10} < 1$ and the wind and wave directions being close to each other.

The comparison of the observed and modeled stress for a pure wind-sea is presented in Fig. 4. The regression line has the slope close to 1 and the bias is almost zero (Fig. 4a). The mean value of $\tau_{\text{mod}}/\tau_{\text{obs}}$ is close to 1 (Fig. 4b). Both r and IOA are high, while the rms error is small. All these suggest that there is an excellent agreement between the calculated and the measured stress for the pure wind-sea case.

TABLE IV Results of comparison. Numbers in brackets are the numbers of nonoutliers

		Nr. of points	τ_{mod}/τ_{obs}	*r*	*rms error*	*IOA*	*Range of* c_p/U_c
Pure wind sea $U_{10} \in [5.79\ 17.19]$ (ms^{-1})		121(121)	1.00 ± 0.19	0.95	0.04	0.98	[0.57 1.00]
Following-swell	All	121(120)	1.13 ± 0.48	0.99	0.00	0.99	[0.86 3.26]
$U_{10} \in [2.35\ 12.60]$	'Stationary' $U_{10} < 6\,\text{ms}^{-1}$	59(58)	1.22 ± 0.63	0.80	0.01	0.87	[1.00 2.99]
	'Stationary' $U_{10} \geq 6\,\text{ms}^{-1}$	51(51)	1.08 ± 0.18	0.99	0.01	0.99	[0.86 1.70]
Cross-swell	All	103(101)	0.90 ± 0.36	0.87	0.03	0.92	[1.00 10.95]
$U_{10} \in [2.46\ 12.29]$	'Stationary' $U_{10} < 6\,\text{ms}^{-1}$	34(34)	0.88 ± 0.37	0.69	0.01	0.70	[1.35 10.95]
	'Stationary' $U_{10} \geq 6\,\text{ms}^{-1}$	49(48)	1.03 ± 0.30	0.81	0.03	0.89	[1.00 2.22]

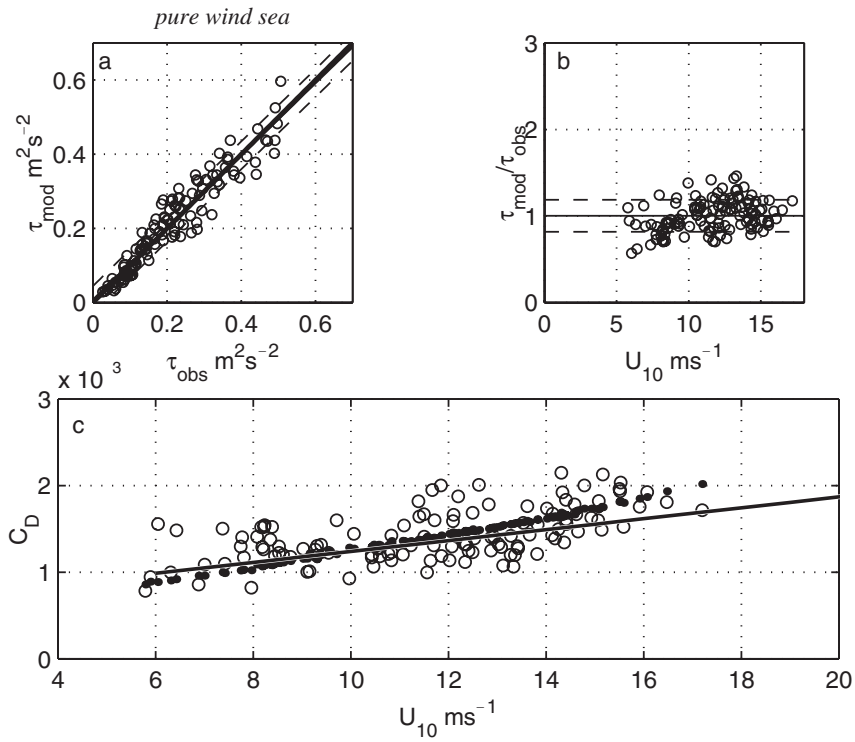

FIGURE 4 Comparison of modeled and measured stress for a pure wind-sea. In (a), the thick solid line is 1 : 1, the thin solid line is the regression line (since the thin solid line is very close to the thick one, it is almost covered by the thick one). The two dashed lines in (a) and (b) represent one standard deviation. (c) C_D is plotted against U_{10} for measurements (○) and model results (●). Solid line is the regression curve from Smith (1980), $C_D = (0.063U_{10} + 0.61) \times 10^{-3}$.

The drag coefficient C_D is plotted against U_{10} in Fig. 4(c). Rings and dots represent the observed and modeled C_D respectively. Notice that the modeled drag coefficient C_D varies with U_{10} with a negligible scatter at a given U_{10}. The agreement is good in the mean over the whole wind speed range. Overall the model results as well as observations show the tendency of increasing drag coefficient with increasing wind speed. For high wind speeds the values of the drag coefficient are slightly higher than that prescribed by the linear regression of C_D by Smith (1980). This increase is explained by KM2001 as a consequence of the airflow separation from breaking short waves. A good comparison between modeled results and data firstly suggests that the main assumption of the model – the constant-flux surface boundary layer – is valid during pure wind-sea conditions. Secondly it indicates that the wave spectrum models used in the model are valid.

4.3 Violation of the Constant-flux Surface Layer Assumption

An example of how the model helped to reveal a specific event in measurements is presented here. When the calculated stress τ_{mod} is plotted against the measured stress τ_{obs} there appears to be a short period when the stress is considerably underestimated by the model while the external parameters (wind speed, significant wave height) do not

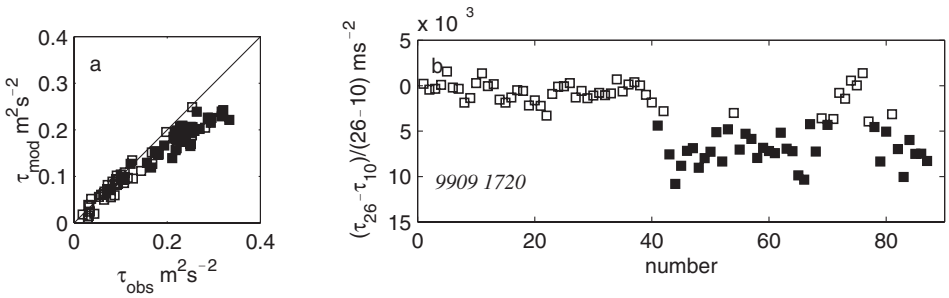

FIGURE 5 One example of measurement being made not in the constant-flux surface layer. (a) τ_{mod} against τ_{obs} (b) Stress divergence between 10 and 26 m, plotted against numbers of hours, continuous in time. Points with relatively larger stress divergence are marked with filled squares.

deviate from those cases for which the model performs well. This period is presented in Fig. 5(a) as the filled symbols. The sea was dominated by relatively young waves. A satellite picture (from the advanced very high-resolution radiometer) shows that there was a front passing at the time of the measurements.

In Fig. 5(b) the vertical divergence of the stress $(\tau_{26} - \tau_{obs})/(26–10)$ between 26 and 10 m is plotted as a time series for this period. It is found that those values with considerably larger stress-divergence (filled symbols) correspond to the underestimated values (filled symbols) in Fig. 5(a). This is an example of measurements taken in the surface layer under the impact of a larger scale phenomenon. The data demonstrate that the condition of the constant-flux surface layer is not fulfilled and thus τ_{obs} does not represent the surface stress. The model based on the constant-flux layer assumption cannot reproduce this case.

4.4 Following-swell

For the following-swell case, U_{10} ranges from $\sim$2 to $\sim$13 ms^{-1}. C_D is plotted against U_{10} in Fig. 6. Data are grouped according to E_1/E_2, $0.2 < E_1/E_2 < 4$ ($\diamond$) – a mixed-sea case, and $E_1/E_2 \geq 4$ ($\diamond$) – a pure swell case, but do not show any specific structure with regards to this grouping. In Fig. 6(a), C_D is calculated from the co-spectra $-\overline{u'w'}$ and $-\overline{v'w'}$ with the cutoff frequency $\sim 10^{-3}$ Hz.

When $U_{10} < 3$ ms^{-1}, C_D values are large, and cannot be explained by the smooth-flow effect. When $-\overline{v'w'}$ is extracted from τ_{obs} and C_D is calculated as $-\overline{u'w'}/\ U_{10}^2$, those large positive values of C_D at light winds disappear. Some of them are moved to large negative values of C_D because $\overline{u'w'} > 0$, as shown in Fig. 6(b). In Fig. 6(b), the distribution of $-\overline{u'w'}/U_{10}^2$ with U_{10} for $U_{10} < 5$ ms^{-1} is very similar to figure 10 in Drennan *et al.* (1999a) for the following swell cases. In Drennan *et al.* (1999a), the turbulent energy spectra and co-spectra of swell runs are compared with those of pure wind-sea runs. It is found that at low frequencies the stress is significantly reduced compared to pure wind-sea values, and can even change the sign. It has also been found that there are significant deviations of the atmospheric spectra from the universal spectral shapes, not only in the mid-range of frequencies (0.06–0.16 Hz) as Rieder and Smith (1998) concluded, but over all frequencies lower than that of the swell. This is also found in Smedman *et al.* (1999).

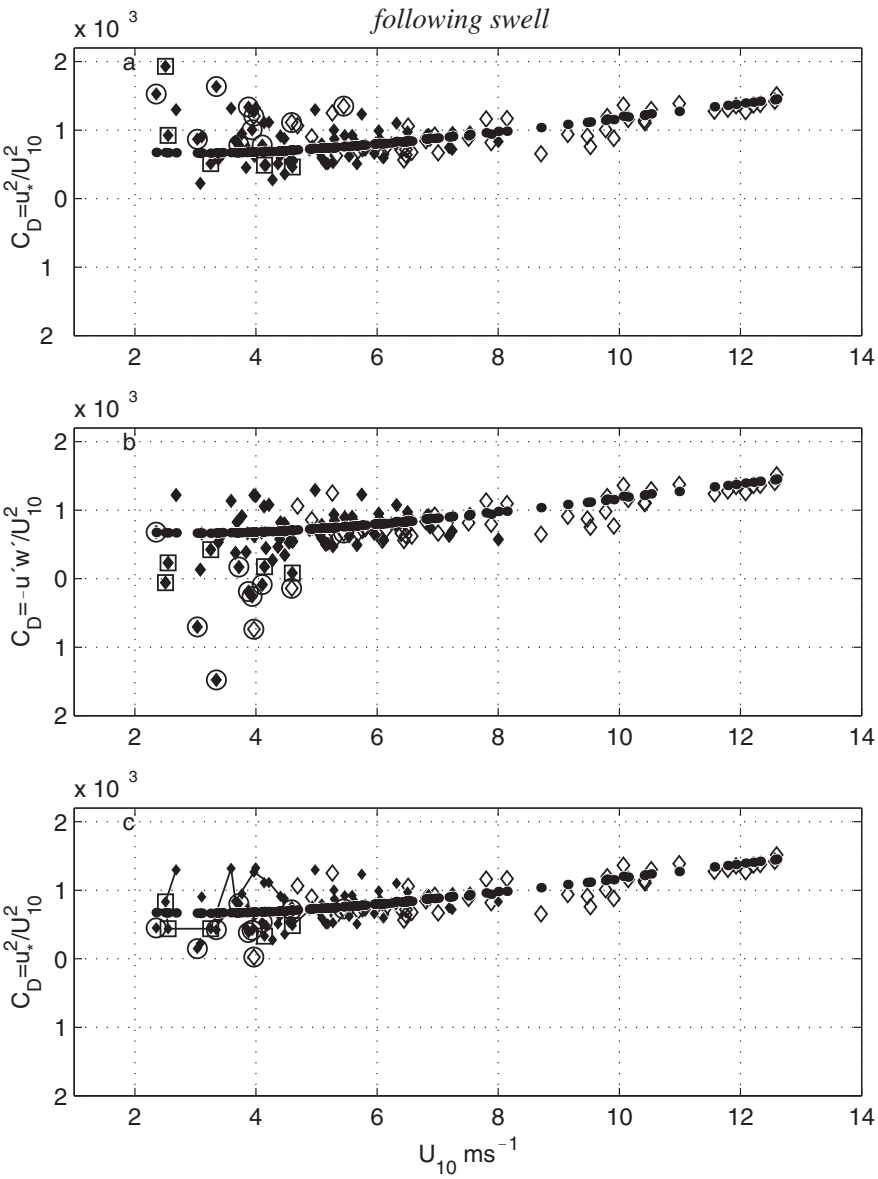

FIGURE 6 C_D plotted against U_{10} for following-swell condition, with measurements presented in categories of E_1/E_2: $0.2 \le E_1/E_2 < 4$ (◇) and $E_1/E_2 \ge 4$ (◆), and modeled values with (•). In subplot (a), C_D is calculated with Eq. (7). In subplot (b), C_D is calculated as $-\overline{u'w'}/U_{10}^2$. In (a) and (b), points marked with (□, 950918) and (○, 960923) have large fluctuations in the co-spectra. In subplot (c) C_D calculated from Eq. (7), $\overline{u'w'}$ and $\overline{v'w'}$ are calculated from the co-spectrum corrected for low frequency noise. Thin solid line linking points in (c) shows 'nonstationary' wind condition.

As mentioned before in Section 2.1, there are several hours of a following-swell condition whose Ogive-curves do not show a plateau at low frequencies. At low frequencies the co-spectra show large irregular fluctuations, which possibly indicate active mesoscale phenomena present in the atmospheric boundary layer. In Fig. 6,

these points are marked with rings (960923, 10 points) and squares (950918, 5 points). Figure 7 gives an example of such co-spectrum of u and w. The small magnitude of $nC_{uw}(n)$ decreases in general towards the peak frequency ~ 0.04 Hz. The irregular fluctuation starts already at around 0.01 Hz.

As a mean of several runs those low frequency fluctuations will bring nothing but scatter. For these 15 runs we cut the co-spectrum at the frequency where the large-scale fluctuation starts and correct the momentum flux in this way. Those points are replaced with their corrected values and are shown in Fig. 6(c). Based on the Ogive-curves, this selected new cutoff frequency would be 0.0085 Hz for run 950918 and 0.0137 Hz for run 960923. For the example in Fig. 7, the corrected $\overline{u'w'}$ value changes from 3.6×10^{-4} to $-2.7 \times 10^{-3}\,\mathrm{m^2 s^{-2}}$.

For $U_{10} < 5\,\mathrm{m\,s^{-1}}$, the scatter has been reduced due to the correction of the stress calculation; however, it is still quite significant. The scatter does not decrease when data are grouped according to $\alpha < 15^\circ$ and $15 \leq \alpha < 30^\circ$. In this low wind regime there is a short period that seems to have the characteristics of the 'nonstationary' wind condition, with wind veering and the wind speed decreasing continuously followed by a slight increase. This short period is marked with a thin solid line in Fig. 6(c) and it adds quite significant variation to C_D. In Smedman *et al.* (2003), case studies of high values of C_D during swell conditions indicate that the history of wave-state, wind speed and direction may be of importance. This 'nonstationary' period is disregarded in the comparison and will be further discussed later.

The modeled C_D values are smaller for swell conditions than that for pure wind-sea conditions. At a given U_{10} the modeled C_D value is quite close to the average measured C_D value, as shown in Fig. 6(c).

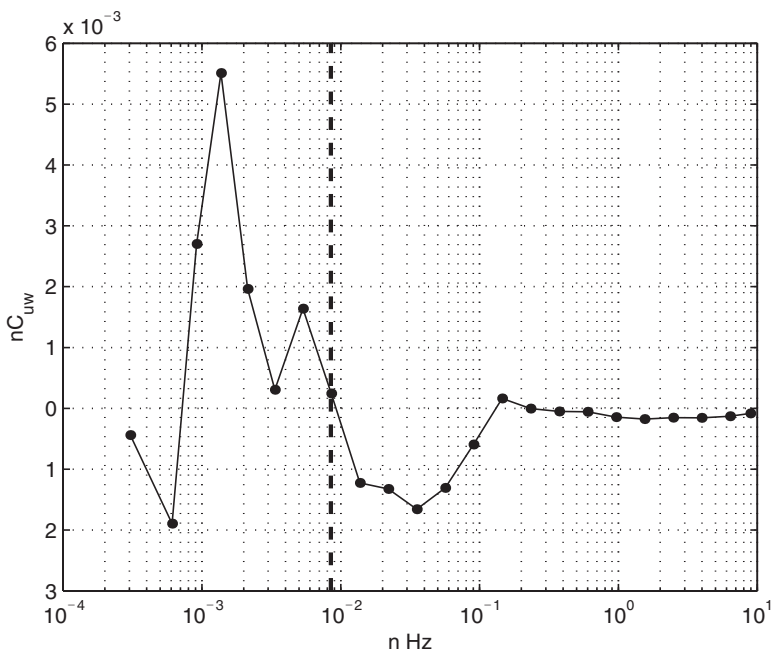

FIGURE 7 Co-spectrum example (19950918 21 : 30) of a following-swell case, with a large fluctuation in the low frequency region. The dashed line shows the new cut-off frequency 0.0085 Hz.

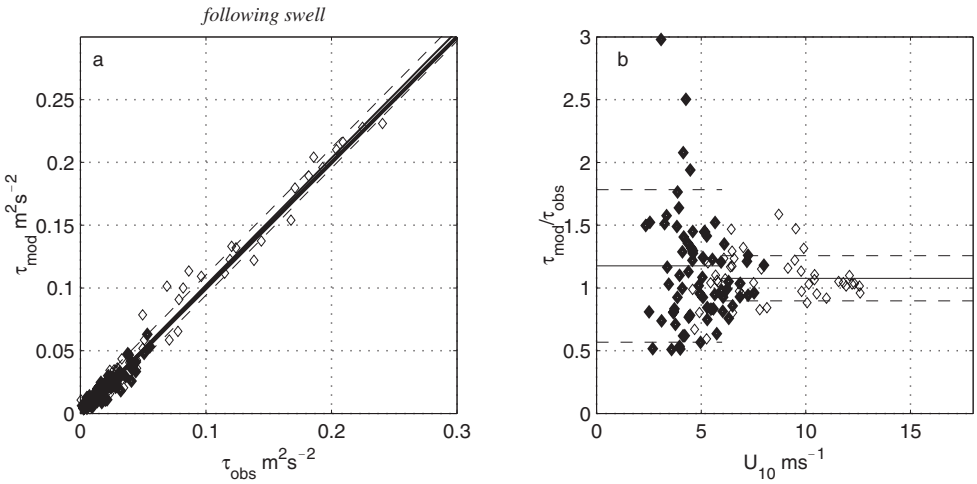

FIGURE 8 Comparison of measured and modeled stress for a following-swell case, in categories of E_1/E_2: $0.2 \le E_1/E_2 < 4$ (◇) and $E_1/E_2 \ge 4$ (◆). In (b), the mean value and standard deviation are calculated for $U_{10} < 6\,\mathrm{ms}^{-1}$ and $U_{10} \ge 6\,\mathrm{ms}^{-1}$respectively. The notation is the same as in Fig. 6(a) and (b).

In Fig. 8(a) the modeled stress is plotted against the measured stress. The regression line has the slope close to 1 and the bias close to 0. The standard deviation is very small. Over the whole range of the stress, the agreement is good between the model and measurements. However, a good agreement in the whole range of stresses, indicated by r and IOA, is simply based on the fact that the calculations of r and IOA are dominated by large values.

A comparison is made for high $U_{10} \ge 6\,\mathrm{ms}^{-1}$ and low $U_{10} < 6\,\mathrm{ms}^{-1}$ wind speeds separately, and the corresponding statistics are given in Table IV. The separation is made at $6\,\mathrm{ms}^{-1}$ to give a clear comparison with the pure wind-sea case, where all points but two are in the range of $U_{10} \ge 6\,\mathrm{ms}^{-1}$. Compared to $U_{10} > 6\,\mathrm{ms}^{-1}$, r and IOA indicate less satisfying agreement between measurements and model for $U_{10} < 6\,\mathrm{ms}^{-1}$.

In Fig. 8(b), the ratio $\tau_{\mathrm{mod}}/\tau_{\mathrm{obs}}$ is plotted against U_{10}. For $U_{10} < 6\,\mathrm{ms}^{-1}$ the standard deviation of the ratio $\tau_{\mathrm{mod}}/\tau_{\mathrm{obs}}$ is much larger than for the pure wind-sea case. In general, the model slightly overestimates the stress for $U_{10} < 6\,\mathrm{ms}^{-1}$. In the light wind regime, there seems to be no direct relation between C_D and U_{10}, as expected. Most data in this region represent a *pure swell* condition when U_{10} and the wind-sea part of the wave field are less relevant.

For $U_{10} \ge 6\,\mathrm{ms}^{-1}$, the mean value and the standard deviation of the stress ratio are comparable to those for the pure wind-sea condition. That suggests that in *these conditions* the stress is provided by the wind-sea part of the whole wave spectrum and the model assumption that swell does not interact with the atmosphere is satisfactory.

Measured values of C_D are overall lower than for pure wind-sea conditions. Drennan *et al.* (1999b) found the same trend but they are unclear whether this difference is due primarily to the presence of following swell, the decay of the wind field, or both.

4.5 Cross-swell

For the cross-swell case, U_{10} ranges from ~2 to ~13 ms^{-1}. In Fig. 9(a) and (c), the modeled stress is plotted against the measured stress. In Fig. 9(b) and (d), the ratio

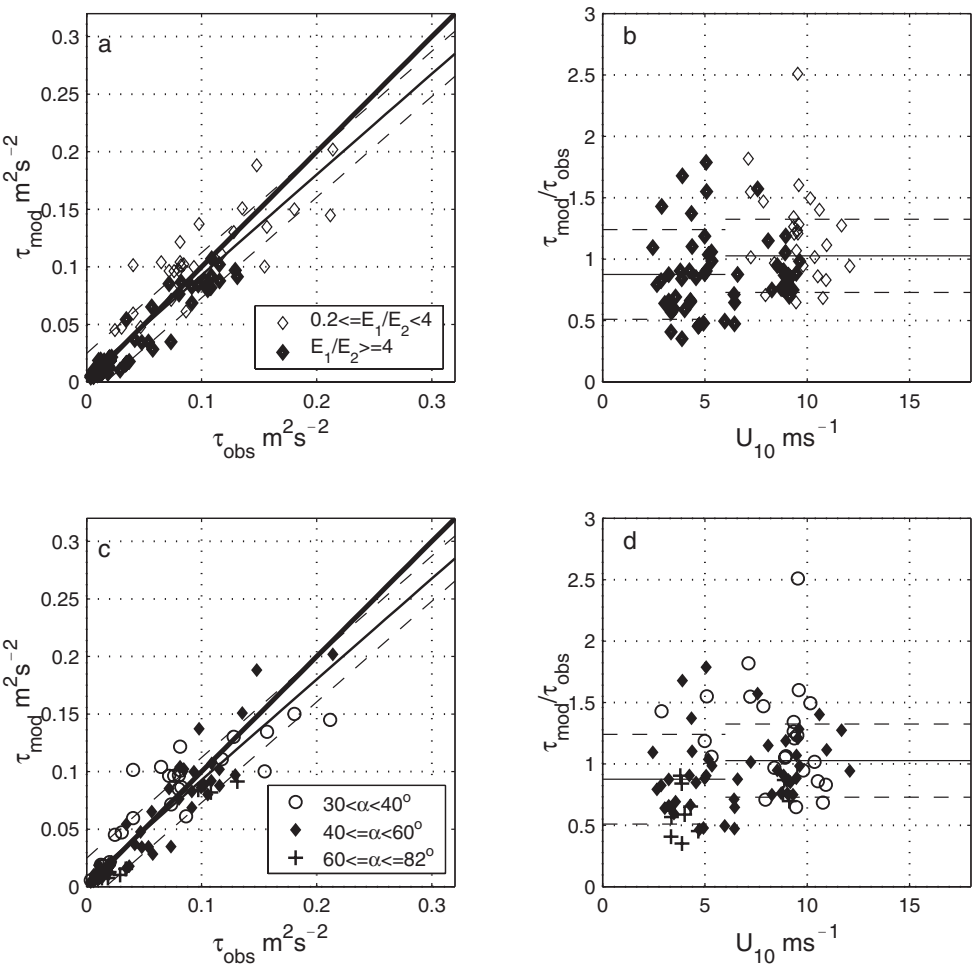

FIGURE 9 Comparison of modeled and measured stress for a cross-swell case, in categories of E_1/E_2 (a and b) and α (c and d). In (b), the mean value and standard deviation are calculated for $U_{10} < 6\,\mathrm{ms}^{-1}$ and $U_{10} \geq 6\,\mathrm{ms}^{-1}$respectively. Notations are the same as those in Fig. 6(a) and (b).

$\tau_{\mathrm{mod}}/\tau_{\mathrm{obs}}$ is plotted as a function of U_{10}, for different E_1/E_2 and α. The overall agreement is reasonable. The standard deviation in Fig. 9(a) and (c) is considerably larger than that for the following-swell case in Fig. 8(a). Statistics (r, rms error and IOA) in Table IV also indicate less satisfying agreement between the model and measurements. The agreement is better for $U_{10} > 6\,\mathrm{ms}^{-1}$ than for $U_{10} < 6\,\mathrm{ms}^{-1}$. The mean value of $\tau_{\mathrm{mod}}/\tau_{\mathrm{obs}}$ is close to 1 for high winds. This result again supports the finding of Donelan *et al.* (1997) and Drennan *et al.* (1999b) that the effect of cross-swell on the sea drag becomes pronounced only for low winds. The model underestimates the drag for low winds and that is in agreement with Donelan *et al.* (1997) and Drennan *et al.* (1999b) who showed that cross-swell increases the drag. Neglecting the effect of swell on the drag in the model seems to be justified for the following-swell and cross-swell under high wind conditions, but not for the cross-swell in the low wind regime.

It is found that there is an extraordinary period when the wind was decreasing continuously for 20 h. This 20-h period was regarded as 'nonstationary' and has been disregarded in the comparison. It is only presented in Fig. 10(a) and will be studied separately later. In Fig. 10(a) C_D is plotted against U_{10} in categories of E_1/E_2 but no specific structure is seen. In Fig. 10(b), the mean values of C_D for each α-group are calculated in U_{10}-bins of $2\,\mathrm{ms}^{-1}$. Figure 10(b) does exhibit the possibility that the drag is enhanced by cross-swell for $U_{10} < 10\,\mathrm{ms}^{-1}$ and suggests that the impact of cross-swell becomes more pronounced with the increase of the angle of swell propagation to the wind. Donelan *et al.* (1997) and Drennan *et al.* (1999a) have observed an even more enhanced drag coefficient due to swell coming across the wind.

The model neglects the impact of swell on the sea drag (α is not taken into account) and it therefore gives the same dependence of C_D on U_{10} as for the following-swell case. The modeled $C_D \sim U_{10}$ curve seems to represent well the data at relatively strong winds. For smaller U_{10}, the model slightly overestimates C_D for $\alpha < 40°$, consistent with Fig. 6(c), but underestimates it for $\alpha > 40°$. The model also underestimates C_D for all data with $\alpha > 60°$. As already was argued above that is in agreement with Donelan *et al.* (1997) and Drennan *et al.* (1999b) who showed that cross-swell increases the drag.

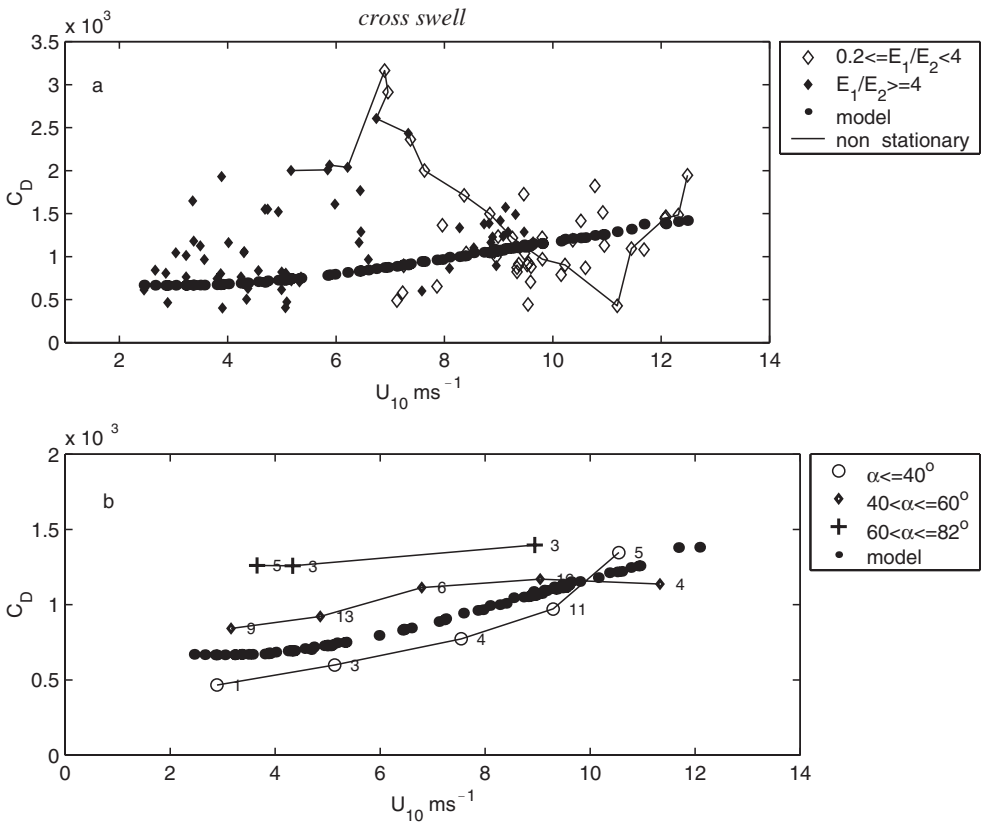

FIGURE 10 (a) C_D plotted against U_{10} for a cross-swell condition, in categories of E_1/E_2. 'nonstationary' hours are marked with thin solid curve. (b) Mean value of C_D against mean U_{10} in U_{10}-bins of $2\,\mathrm{ms}^{-1}$, in categories of α, number of points in each U_{10}-bin is given. In (b), 'nonstationary' hours are not included.

In Fig. 11, C_D for three cases (a pure wind-sea, following-swell and cross-swell cases) are plotted against U_{10}. In spite of the fact that there is significant scatter at light winds, the mean values of C_D and U_{10} are calculated for U_{10}-interval of $2\,\mathrm{ms}^{-1}$: $\langle C_D\rangle_j$ and $\langle U_{10}\rangle_j$, where j represents the jth interval of U_{10}. The error-bars are the confidence intervals for $\langle C_D\rangle_j$ and they are defined as: $\sigma_j/\sqrt{N_j}$ where σ_j and N_j are the standard deviation of C_D and the number of points at the jth U_{10}-interval. In general, data in each U_{10}-interval satisfy the 'normal distribution', i.e. $\sim 67\%$ of the data are within one standard deviation, and $\sim 95\%$ of the data are within two standard deviation.

It is shown statistically in Fig. 11 that the differences between three cases are small for $U_{10} > 10\,\mathrm{ms}^{-1}$. For $U_{10} < 10\,\mathrm{ms}^{-1}$ the average drag is smaller in general for the *swell* case than for the pure wind-sea case. In Donelan *et al.* (1997) the enhanced drag is found to be larger than that during pure wind-sea condition. This is probably due to the fact that their data have, for the most part, a counter-swell component; in the present study the largest value of α is $\sim 82^\circ$ and for the most part the data have a following-swell component. The magnitude as well as the scatter of C_D at given U_{10}-interval is larger for the cross-swell case than for the following-swell case. Together with Fig. 10 this demonstrates the role played by the wind-cross-swell effect: it enhances the drag.

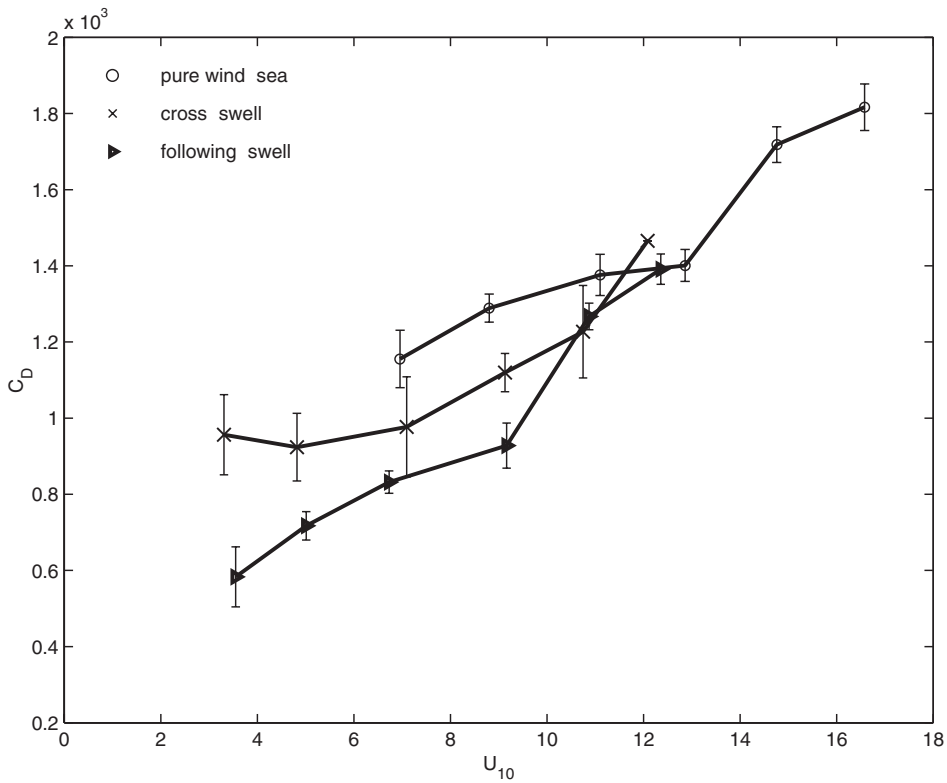

FIGURE 11 Mean values of C_D against mean values of U_{10} in U_{10}-bins of $2\,\mathrm{ms}^{-1}$, for a pure wind-sea, following-swell and cross-swell respectively. Error-bars give the confidence intervals for the mean values of C_D.

4.6 'Nonstationary' Condition

The impact of the flow acceleration (deceleration) is expected to cause larger (smaller) drag coefficient for a given wind speed since the flow acceleration is usually accompanied by developing young waves, as observed by (for example) Smith (1980), while the flow deceleration is usually accompanied by the mature sea and swell, as observed by Smedman *et al.* (1999). Drennan *et al.* (1999b) observed that with a wind-decay from about 9 to about 4.5 ms^{-1}, C_D decreased from about 1.2×10^{-3} to 0.5×10^{-3}. They conclude that "it is unclear whether this difference is due primarily to the presence of following swells, the decay of the wind field, or both". Vickers and Mahrt (1997) compared the drag coefficient as a function of the wind speed for off- and on-shore flow and found no significant difference between accelerating and decelerating cases. They conclude that "this is probably due to the fact that, for these data, flow acceleration only occasionally determines the wave state". In other words, wave-state is considered more appropriate in determining the drag coefficient.

The periods of 'nonstationary' wind condition in both following-swell (Fig. 6c) and cross-swell (Fig. 10a) cases correspond to a large amplitude of the fluctuation of C_D. In order to find out how C_D reacts to a 'nonstationary' wind field, a pure wind-sea period is also selected with a variation in U_{10}, which is comparable to the cross-swell case. Some of the mean variables during these three periods are given in Table V. In Fig. 12 (pure wind-sea), Fig. 13 (following-swell) and Fig. 14 (cross-swell) three periods are inserted into longer time series of U_{10} and c_p (subplot-a), of wind and dominant wave directions (subplot-b), of observed and modeled C_D (subplot-c) and of u_* (subplot-d). In Figs. 12–14, those points marked with rings correspond to $\alpha < 30°$. For all periods the wind speed varies by less than 1 ms^{-1} per hour, and wind veers by less than 17° per hour. Thus the definition of 'nonstationarity' is rather tentative.

For the pure wind-sea period, the wind is quite strong and it increases with time continuously. Correspondingly, C_D follows the trend of U_{10} and increases slightly. Comparing the variation of U_{10} and u_* one can find that for the pure wind-sea case u_* varies in phase with U_{10} indicating a close relationship between the local wind and stress, as expected.

For the following-swell period, the wind is rather weak and decreases slightly with time. The wind is originally across swell, but it veers, coincides with the direction of long waves, and veers again to be across swell. Compared with the periods of pure wind-sea and cross-swell conditions, wind and wave change their direction more rapidly, and, although the mean value of C_D is the smallest, C_D fluctuates most rapidly. For the following-swell case, u_* is of very small magnitude. The small

TABLE V Some mean variables for three events of a 'nonstationary' wind field for a pure wind-sea, following-swell and cross-swell cases

	Pure wind-sea	*Following-swell*	*Cross-swell*
Date and Time	1998-03-26 18 : 30–03-27 13 : 30	1995-09-18 12 : 30–22 : 30	1998-11-12 3 : 30–22 : 30
Mean U_{10}	11.40 ms^{-1}	3.66 ms^{-1}	8.60 ms^{-1}
Mean dU_{10}/dt	0.384 $ms^{-1}\,h^{-1}$	−0.232 $ms^{-1}\,h^{-1}$	−0.388 $ms^{-1}\,h^{-1}$
Mean C_D	1.33×10^{-3}	0.88×10^{-3}	1.81×10^{-3}
Mean dC_D/dt	$0.12 \times 10^{-3}\,h^{-1}$	$0.33 \times 10^{-3}\,h^{-1}$	$0.27 \times 10^{-3}\,h^{-1}$
Mean d(wind dir.)/dt	3.05° h^{-1}	8.84° h^{-1}	4.25° h^{-1}
Mean d(wave dir.)/dt	2.79° h^{-1}	6.64° h^{-1}	5.45° h^{-1}

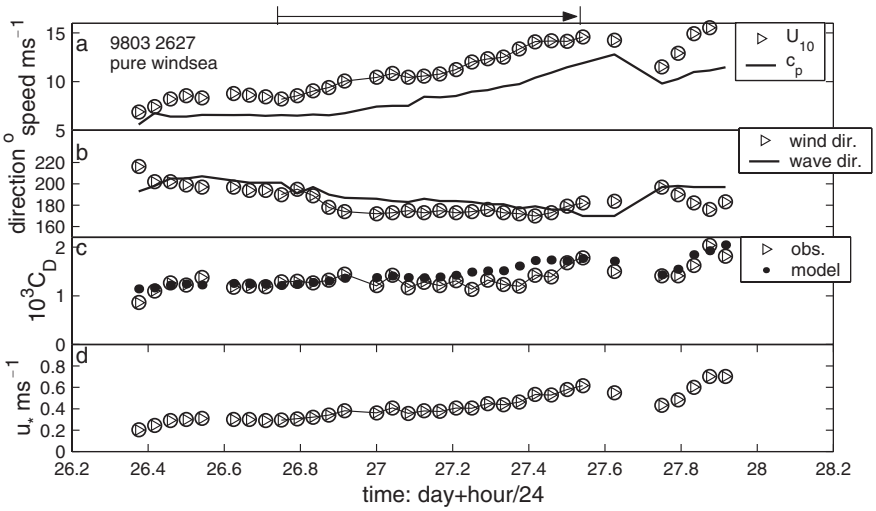

FIGURE 12 Time series containing a 'nonstationary' pure wind-sea period. The 'nonstationary' period is linked with thin solid curve in each subplot, and it is also marked with a arrow on the top of the figure. (a) U_{10} and c_p, (b) directions of wind and dominant waves, (c) observed and modeled C_D, (d) observed u_*. In Figs. 12–14, points marked with (o) correspond to $\alpha < 30^\circ$.

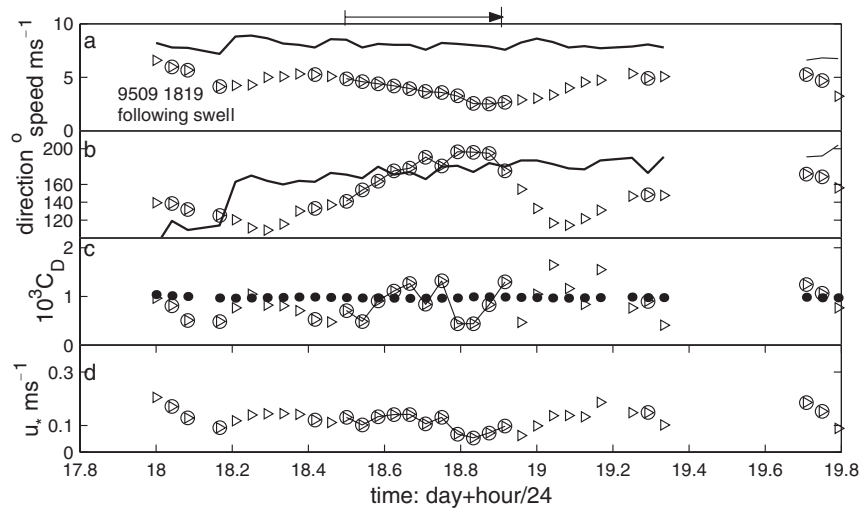

FIGURE 13 Time series containing a 'nonstationary' following-swell period. This 'nonstationary' period is also marked in Fig. 8(c). Notations are the same as those in Fig 12.

variation in u_* is sufficient to lead to a large fluctuation of C_D, since the wind speed is also small. At the end of day-18 and beginning of day-19 the wind direction changes, the following-swell turns to cross-swell and C_D increases as shown in the previous subsection.

For the cross-swell period, the wind is rather strong and the wind speed remains the same as at the beginning. It decreases continuously from 12.5 to 5.2 ms^{-1} during the last 20 h. The drag coefficient, being almost constant in the first stage, increases rapidly in the second. This rapid increase is explained by a decrease of the wind speed, as the

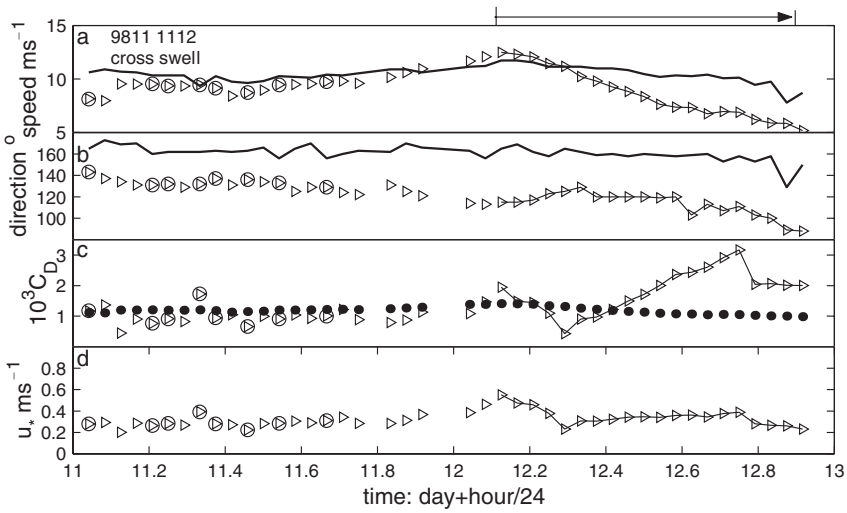

FIGURE 14 Time series containing a 'nonstationary' cross-swell period. This 'nonstationary' period is also marked in Fig. 12(a). Notations are the same as those in Fig 12.

friction velocity remains almost constant. This suggests that the relation between u_* and U_{10} for this swell case is weak, and the sea drag is supported by cross-swell by a mechanism yet unknown.

The model calculates the drag well for the 'nonstationary' pure wind-sea period but it is not able to capture the variation of the drag for the two *swell* periods.

The wind speed variation explains very little of the difference in the variation of C_D for the swell periods. Neither can the magnitude of acceleration/deceleration alone predict the variation of C_D. The interaction between swell, wind waves and the atmosphere, the mechanism of which is not yet clear, appears to lead to the complicated variation of C_D.

5 CONCLUSIONS

The wave impact on the sea drag has been studied by using meteorological measurements from an air–sea interaction station situated on the island Östergarnsholm, wave data from a wave buoy moored in the Baltic Sea outside the island, and simulation from a WOWC model. The study has been carried out for different sea states, namely a pure wind-sea, following-swell/mixed sea and cross-swell/mixed sea, and it demonstrates that the surface stress (or sea drag, or roughness length) is dependent on sea-state.

The present study does reveal that the impact of swell on the sea drag is well pronounced at low wind speeds. The model reproduces very well the measured stress in pure wind-sea conditions and in mixed wind-sea/swell conditions at moderate to high wind speeds, but fails to capture the peculiarities of the exchange at low wind speeds in presence of swell. However, the model helped to distinguish these peculiarities and it proves to be a useful tool in the interpretation of the data.

For following-swell cases, the measured values of the drag coefficient C_D are lower overall than that for pure wind-sea cases, consistent with the study of Drennan *et al.*

(1999a,b). The measurements show that the drag is enhanced by cross-swell for the wind speed $U_{10} < 10\,\mathrm{ms}^{-1}$ supporting the finding of Donelan *et al.* (1997) and Drennan *et al.* (1999b). The impact of cross-swell becomes more pronounced as the angle between the swell propagation and the wind direction increases (up to 82° in the present study).

For a pure wind-sea there is a good agreement between the model results and measurements. Both the model and observations show an increasing trend of the drag coefficient C_D with increasing wind speed U_{10}, compared to a linear regression of C_D with U_{10}. This increase is explained by the model as a consequence of the airflow separation from breaking short waves.

When the modeled and measured stress is compared with each other, it is expected that both of them represent the stress in the constant-flux surface layer. A good agreement between modeled and measured stress suggests that this condition be fulfilled. Under the impact of a large-scale atmospheric boundary layer phenomenon, the model helped to reveal the fact that sometimes the measurements were not taken in the constant-flux surface layer.

In general for swell-dominated cases, the agreement between the average values of the modelled and measured stress is good for $U_{10} > 6\,\mathrm{ms}^{-1}$, where most of data represent a mixed sea. The model neglects the impact of swell on the stress. A good comparison suggests that in these conditions the stress is mainly provided by the wind-sea part of the whole spectrum and the model assumption of no-influence from pure swell is appropriate.

For $U_{10} < 6\,\mathrm{ms}^{-1}$, the agreement between the model and measurements becomes much less satisfying. Most data represent pure swell conditions and the scatter is large. In general, for $U_{10} < 6\,\mathrm{ms}^{-1}$, when swell energy occupies most part of the wave spectrum, the model overestimates the stress for the following-swell case. For the cross-swell case, the model has not taken wind-cross-swell effects into account and gives the same result as that for the following-swell case. This leads to an underestimation of stress for larger α.

During pure swell conditions, data are characterized by a large variation of the drag coefficient. Further study is needed to find out the reasons why following swell reduces drag. However, the variation of drag coefficient during pure swell conditions is found to be caused by the mesoscale variability in the atmospheric boundary layer revealed in the stress co-spectra, wind-cross-swell effects and nonstationarity in the wave and wind fields. This suggests that when estimating surface stress during pure swell conditions, further studies are needed to find out the origin of low frequency fluctuations in the stress co-spectra and the proper cutoff frequency; the mechanism of the drag enhancement under wind-cross-swell conditions; the mechanism of the interaction between swell, wind waves and the atmosphere, which leads to the complicated variation of C_D for the 'non-stationary' periods of swell conditions.

Acknowledgment

The work was partly funded by the European Union, within the project SFINCS, ENV4-CT97-0573. We would like to thank Hans Bergström and other members of the MIUU staff for providing the measurements, and thank Dr. Kimmo Kahma and Heidi Pettersson at the Finnish Institute of Marine Research for the wave data.

The second author acknowledges the support by the Netherlands Organization for Scientific Research (NWO) through the Dutch-Russian Scientific Co-operation Programme 2001, project number 047.014.009 and by EU INTAS – International Association – under grant INTAS-2001-2132.

References

Dobson, F.W., Smith, S.D. and Anderson, R.J. (1994). Measuring the relationship between wind stress and sea state in the open ocean in the presence of swell. *Atmosphere-Ocean*, **32**(1), 237–256.

Donelan, M.A., Drennan, W.M. and Katsaros, K.B. (1997). The air-sea momentum flux in conditions of wind sea and swell. *J. Phys. Oceanogr.*, **27**, 2087–2099.

Donelan, M.A., Hamilon, J. and Hui, W.H. (1985). Directional spectra of wind-generated waves. *Phil. Trans. R. Soc. London*, A **315**, 509–562.

Donelan, M.A. (1990). Air-sea interaction. In: *The Sea*: *Ocean Engineering Science*, Vol. 9, pp. 239–292.

Drennan, W., Kahma, K.K. and Donelan, M.A. (1999a). On momentum flux and velocity spectra over waves. *Boundary-Layer Meteorol.*, **92**, 489–515.

Drennan, W., Graber, H.C. and Donelan, M.A. (1999b). Evidence for the effects of swell and unsteady winds on marine wind stress. *J. Phys. Oceanogr*, **29**, 1853–1864.

Geernaert, G.L. (1990) Bulk parameterization for the wind stress and heat fluxes. In: Geernaert, G.L. and Plant, W.J. (Eds.), *Surface Waves and Fluxes*, 336 pp. Kluwer Academic, Norwell, Mass.

Grachev, A.A. and Fairall, C.W. (2001). Upward momentum transfer in the marine boundary layer. *J. Phys. Oceanogr.*, **31**, 1698–1711.

Grelle, A. and Lindroth, A. (1994). Flow distortion by a solent sonic anemometer: wind tunnel calibration and its assessment for flux measurements over forest and field. *J. Atmos. Oceanic Technol.*, **11**, 1529–1542.

Kudryavtsev, V.N. and Makin, V.K. (2001). The impact of air-flow separation on the drag of the sea surface. *Boundary-Layer Meteorol.*, **98**, 155–171.

Kudryavtsev, V.N., Makin, V.K. and Chapron, B. (1999). Coupled sea surface-atmosphere model 2. spectrum of short wind waves. *J. Geophys. Res.*, **104**, 7625–7639.

Makin, V.K. and Kudryavtsev, V.N. (2002). Impact of dominant waves on sea drag. *Boundary-Layer Meteorol.*, **103**, 83–99.

Plant, W.J. (1982). A relation between wind stress and wave slope. *J. Geophys. Res.*, **87**, 1961–1967.

Rieder, K.F. and Smith, J.A. (1998). Removing wave effects from the wind stress vector. *J. Geophys. Res.*, **103**, 1363–1374.

Rieder, K.F. (1997). Analysis of sea-surface drag parameterizations in open ocean conditions. *Boundary-Layer Meteorol.*, **82**, 355–377.

Sjöblom, A. and Smedman, A. (2002). The turbulence budget in the marine atmospheric surface layer. *J. Geophys. Res.*, **107**(C10), 3142, doi: 10.1029/2001JC001016.

Smedman, A.-S., Guo-Larsén, X., Högström, U., Kahma, K.K. and Pettersson, H. (2003). The effect of sea state on the momentum exchange over the sea during neutral conditions. *J. Geophys. Res.* (accepted).

Smedman, A.-S., Högström, U., Bergström, H., Rutgersson, A., Kahma, K.K. and Pettersson, H. (1999). A case study of air-sea interaction during swell conditions. *J. Geophys. Res.*, **104**, 25833–25851.

Smith, S.D. (1980). Wind stress and heat flux over the ocean in Gale force winds. *J. Phys. Oceanogr.*, **10**, 709–726.

Smith, S.D., Fairall, C.W., Geernaert, G.L. and Hasse, L. (1996). Air-sea fluxes: 25 years of progress. *Boundary-Layer Meteorol.*, **78**, 247–290.

Snodgrass, F.E., Groves, G.W., Hasselmann, K.F., Miller, G.R., Munk, W.H. and Powers, W.H. (1966). Propagation of ocean swell across the Pacific. *Phil. Trans. Roy. London*, **A 259**, 431–497.

Vickers, D. and Mahrt, L. (1997). Fetch limited drag coefficients. *Boundary-Layer Meteorol.*, **85**, 53–79.

Willmott, C.J., Ackleson, S.G., Davis, R.E., Feddema, J.J., Klink, K.M., Legates, D.R., O'Donnell, J. and Rowe, C.M. (1985). Statistics for the evaluation and comparison of models. *J. Geophys. Res.* **90**, 8995–9005.

APPENDIX

Statistical Parameters

The correlation coefficient (r) is calculated as

$$r = \frac{(X_o - \overline{X_o})(X_m - \overline{X_m})}{\sigma_o \sigma_m}$$

where X_o is the observed variable, and X_m is the modeled variable. Overbars represent averages over the whole data set. The standard deviations of the observed and modeled variables σ_o and σ_m are

$$\sigma_o = \left(\frac{1}{N} \sum_{i=1}^{N} (X_o - \overline{X_o})^2 \right)^{1/2}$$

$$\sigma_m = \left(\frac{1}{N} \sum_{i=1}^{N} (X_m - \overline{X_m})^2 \right)^{1/2}$$

where N is the number of data points.

The root mean square error (rms error) is calculated as

$$\text{rms error} = \left(\frac{1}{N} \sum_{i=1}^{N} (X_o - X_m)^2 \right)^{1/2}$$

The 'index of agreement (IOA)' is adopted from Wilmott *et al.* (1985):

$$IOA = 1 - \frac{\sum_{i=1}^{N} (X_o - X_m)^2}{\sum_{i=1}^{N} (|X_m - \overline{X_o}| + |X_o - \overline{X_o}|)^2}$$